DOI: 10.1002/cssc.201100618

Three-Dimensional Hierarchically Ordered Porous Carbons with Partially Graphitic Nanostructures for Electrochemical Capacitive Energy Storage

Chun-Hsien Huang,[a, b] Qiang Zhang,[b, c] Tsu-Chin Chou,[a] Cheng-Meng Chen,[b, d] Dang Sheng Su,*[b, e] and Ruey-An Doong*[a]

Three-dimensional, hierarchically ordered, porous carbon (HOPC) with designed porous textures, serving as an ion-buffering reservoir, an ion-transport channel, and a charge-storage material, is expected to be advanced an energy material for high-rate supercapacitors. Herein, HOPC without/with partially graphitic nanostructures have been directly synthesized by means of a simple one-pot synthesis procedure. The designed porous textures of the 3D HOPC materials are composed of highly ordered, fcc macroporous (300 nm), interconnected porous structures, including macroporous windows (170 nm), hexagonally ordered mesopores (5.0 nm), and useful micropores (1.2 nm). 3D HOPC-g-1000 (g = graphitic, 1000 = pyrolysis temperature of 1000 °C) with partially graphitic nanostructures has a low specific surface area (296 $m^2 g^{-1}$) and a low gravimetric specific capacitance (73.4 $F g^{-1}$ at 3 $mV s^{-1}$), but improved electrical conductivity, better rate performance, higher electrolyte accessibility (24.8 $\mu F cm^{-2}$ at 3 $mV s^{-1}$), faster frequency response ($\approx$1 Hz), and excellent cycling performance (> 5400 cycles). The specific capacitance per surface area is higher than that of conventional porous carbons, carbon nanotubes, and modified graphene (10–19 $\mu F cm^{-2}$).

Introduction

Supercapacitors with power densities exceeding 1 $kW kg^{-1}$ and long cyclic lives have recently attracted considerable attention because of the vast potential in portable electronics, hybrid electric vehicles, and large industrial equipment.[1–6] Despite this high power density, current supercapacitors have lower energy densities than batteries. The performance can be substantially improved with the aim of increasing the energy density and improving capacitance retention at a high discharge rate, while retaining the high power density and long cycling life. The fabrication of amenable materials to define the relationship between performance and the specific porous structure of electrode materials is valuable.

To meet these requirements of electrode materials with high charge storage capacitance, better electrolyte accessibility, excellent electrical conductivity, and effective ion-transport pathways are needed. Among these parameters, accessible surface area, porous structure, and electrical conductivity appear to be the most important factors.[2,5–7] Carbons such as activated carbon, ordered mesoporous carbon (OMC), hierarchically porous carbon, carbide-derived carbon, graphene, carbon nanotubes (CNTs), and carbon nanofibers are the most promising candidates and have previously been utilized for electrochemical energy storage because of their unique physicochemical properties.[2–18] Activated carbons are typical electrode materials with high surface areas and high microporosities for supercapacitors.[4,10,19] However, their storage performance deteriorates dramatically at high discharge rates due to low conductivity (8.5×10^{-5} $S cm^{-1}$), high ion-transport resistance, and poor electrolyte accessibility within their tortuous microporous channels.[20,21] OMC with extremely high surface area, controllable pore size (3–7 nm), and interconnected channel structure exhibits a much lower ion-transport resistance.[22–25] However, the specific porous textures of OMC cannot improve on the high rate (< 2 s) performance of supercapacitors. It is noteworthy that 3D, aperiodic, hierarchically porous graphitic carbon has been developed for high-rate supercapacitors.[8] Recently, 3D hierarchically porous carbons, which have hollow macroporous cores surrounded by three different thicknesses of mesoporous shells, were developed for a systematic investigation of

[a] C.-H. Huang, T.-C. Chou, Prof. R.-A. Doong
Department of Biomedical Engineering and Environmental Sciences
National Tsing-Hua University, Hsinchu 30013 (Taiwan)
Fax: (+886) 3-5718649
E-mail: radoong@mx.nthu.edu.tw

[b] C.-H. Huang, Dr. Q. Zhang, C.-M. Chen, Dr. D. S. Su
Department of Inorganic Chemistry
Fritz Haber Institute of the Max Planck Society
Faradayweg 4–6, Berlin 14195 (Germany)
E-mail: dangsheng@fhi-berlin.mpg.de

[c] Dr. Q. Zhang
Department of Chemical Engineering, Tsinghua University
Beijing 100084 (P.R. China)

[d] C.-M. Chen
Key Laboratory of Carbon Materials
Institute of Coal Chemistry, Chinese Academy of Sciences
Taoyuan South Road 27, Taiyuan 030001 (P.R. China)

[e] Dr. D. S. Su
Shenyang National Laboratory for Materials Science
Institute of Metal Research, Chinese Academy of Science
72 Wenhua Road, Shenyang 110016 (P.R. China)

Supporting Information for this article is available on the WWW under http://dx.doi.org/10.1002/cssc.201100618.

capacitance and ion transport.[26] However, these hierarchically porous structures are not ordered and lack macroporous windows to interconnect macropores. The fabrication of graphitic carbons with hierarchically porous structures is of interest for use as electrode materials.[8,27–29] With the aid of suitable templates, hierarchically porous carbon materials with designed porosity were achievable.[8,17,22,24,29–32] The fabrication of 3D, hierarchically ordered, porous carbons with partially graphitic nanostructures (HOPC-g) usually involves two steps: formation of a highly ordered opal structure followed by infiltration of carbon precursors into the voids in the opal structure to solidify the porous structure. To generate graphitic carbon, catalytic pyrolysis of carbon precursors in the presence of transition metals is one commonly used method.[29,33,34]

Herein, the dual-templated synthesis and electrochemical performance of 3D HOPCs without/with partially graphitic nanostructures were fabricated for electrochemical capacitive energy storage. Polystyrene (PS) latex spheres (512 nm) and triblock copolymer F127 ($EO_{106}PO_{70}EO_{106}$) were employed as macro- and mesoporous templates, while phenol–formaldehyde (PF) resins and Ni species were added as the carbon source and graphitization catalyst, respectively.[28] The designed porous structure of 3D HOPC-g materials with well-crystallized graphitic carbons were composed of highly ordered fcc macropores (300 nm); interconnected porous structures, including macroporous windows (170 nm); hexagonally ordered mesopores in the frameworks; and useful micropores. The macropores, interconnected porous structures, and meso- (5.0 nm)/micropores (1.2 nm) were used as ion-buffering reservoirs, ion-transport channels, and as charge-storage materials, respectively. The 3D HOPCs without/with graphitic nanostructures have significant effects on the kinetics of electrical double-layer formation due to the enhanced permeation of electrolytes through the porous structures, the transport of both ions and electrons, and better electrolyte accessibility. It is a useful platform to clarify transport limitation and the roles of ordered pores and graphitic nanostructures in sustainable catalysis, catalyst supports, and energy storage.

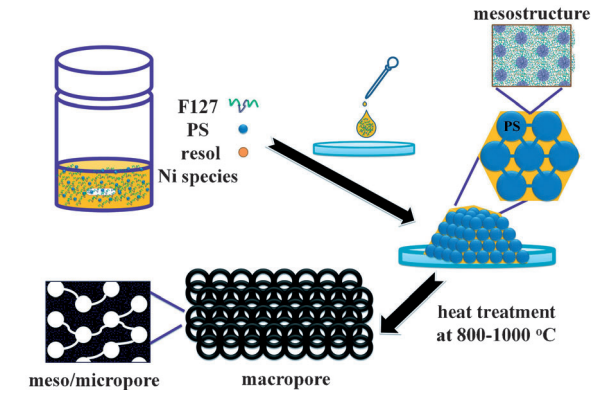

Scheme 1. Illustration of the synthetic routes to 3D hierarchically ordered porous carbon through one-pot and evaporation-induced self-assembly.

Results and Discussion

Synthesis and characterization of 3D HOPC materials

PS latex spheres, serving as template for macropores in the synthesis of 3D HOPC materials, have a uniform particle size of (512 ± 5) nm (Figure S1 in the Supporting Information). After removal of F127 and PS templates by heat treatment at 800 and 1000 °C, respectively, 3D HOPC materials with well-interconnected macroporous structures were formed (Scheme 1). Detailed synthetic strategies are described in our previous study.[29] The method developed herein has several unique features compared with reported synthesis strategies:[29–32,35] 1) the direct synthesis of 3D HOPC circumvents the pre-preparation of 3D crystal arrays and the use of silica and hazardous hydrofluoric acid, making the current method more environmentally benign; 2) the size of the macropores and the symmetries of the mesostructures can be easily tuned by simply changing the size of PS spheres and ratio of PF resins and F127; and 3) the graphitic structures in the materials can be obtained at a low pyrolysis temperature of 1000 °C, which is much lower than the high graphitization temperature of 2000 °C.

The obtained 3D HOPC materials were denoted HOPC-800 and HOPC-g-1000, in which g represents graphitic nanostructure, and 800 and 1000 refer to the pyrolysis temperatures. The macropore size and macroporous window size of HOPC-g-1000 are about 300 and 170 nm, respectively (Figure 1 a). The interior structure of HOPC-g-1000 was analyzed by performing TEM (Figure 1 b–d and Figure S2 in the Supporting Information). Regularly patterned, well-interconnected macroporous structures and 2D, hexagonally ordered mesostructures in the carbon framework are clearly observed. The cylindrical mesopore channels are oriented along with the curvature of macropore wall surface (Figure 1 c).

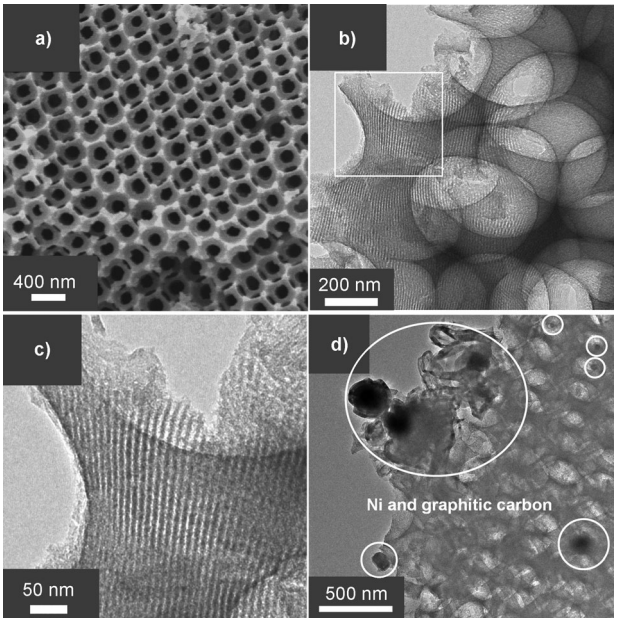

Figure 1. a) SEM and b–d) TEM images of HOPC-g-1000. c) An enlargement of the image shown in part b).

The small-angle XRD pattern of HOPC-g-1000 confirms the generation of ordered mesostructures in the framework. The XRD pattern of HOPC-g-1000 shows a major and small diffraction peak at $2\theta = 0.93^\circ$ (Figure S3 in the Supporting Information), which can be assigned as the (10) reflection of 2D hexagonal mesostructures.[31] The cell parameter (a_o), calculated from the (10) scattering peak by using the formula $a_0 = 2d_{10}/\sqrt{3}$, is 11 nm. The small diffraction peak resulted from the small domain of ordered structures and channel distortions observed in the TEM image (Figure 1b and c); this observation is consistent with previous results.[29,31,32]

Wide-angle XRD patterns of HOPC-800 and HOPC-g-1000 are shown in Figure 2. The three resolved diffraction peaks (2θ) at

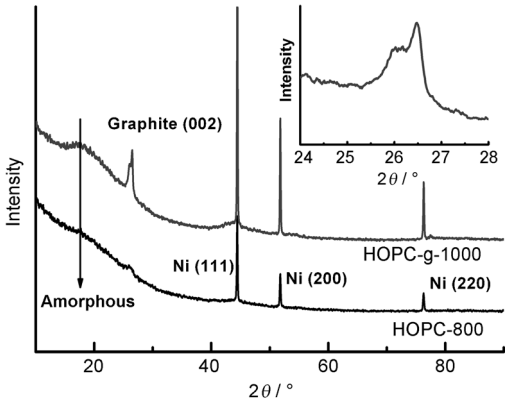

Figure 2. Wide-angle XRD patterns of HOPC-800 and HOPC-g-1000.

44.4, 51.8, and 76.3°, assigned as the (111), (200), and (220) reflections of fcc metallic Ni (JCPDS 04-0850), respectively, are observed for HOPC-800. The wide-angle XRD pattern of HOPC-g-1000 clearly shows characteristics of amorphous carbon, graphite, and metallic Ni. The diffraction peaks at $2\theta = 26.0$ and 26.5°, which can be assigned as the (002) reflection of graphite, correspond to a turbostratic structure (T-rich) and graphitic carbon (G-rich), respectively. T-rich carbon is an intermediate between ideal graphite and amorphous carbon.[36,37] The interplanar distance of d_{002} and the mean stacking thickness of graphite domains for G-rich carbon are 0.336 and about 20 nm, respectively. In addition, the graphitization degree parameter (g) is employed to quantify the degree of similarity between the carbon material and a perfect single crystal of graphite. The g value of G-rich carbon, estimated from the equation $g = (0.344 - d_{002})/0.0086$, is 0.93 and indicates the formation of a well-developed graphitic structure at 1000 °C under an H_2/N_2 atmosphere in the presence of Ni.[29]

The dark metallic Ni nanoparticles are embedded in the carbon framework, and a turbostratic thin layer of graphitic carbon on the surface of metallic Ni is discernible (Figure 1d and Figure S2 in the Supporting Information), confirming the catalytic graphitization process. The formation of graphitic structures around the surface of metallic Ni occurs through the dissolution of amorphous carbon into the Ni particles, followed by surface diffusion of carbon atoms, and finally assembly into

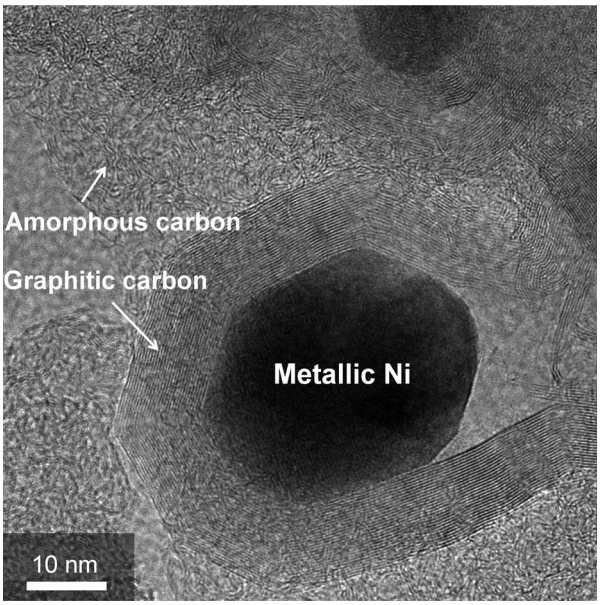

Figure 3. High-resolution TEM image of HOPC-g-1000.

graphitic carbon, which is similar to graphitic CNT growth on metal particles.[29,38–40] As shown in the high-resolution TEM image of HOPC-g-1000 (Figure 3), the total width of these graphitic carbons is about 12 nm, and the distance between graphite layers is 0.340 nm, which is in good agreement with the XRD pattern results. There are short domains of parallel, single-layer graphene sheets in the carbon framework. These results clearly indicate that HOPC-g-1000 material contains amorphous and graphitic carbon in the framework.

Complementary electronic information is provided by carbon K-edge X-ray absorption near-edge spectroscopy (XANES) for graphite, HOPC-800, and HOPC-g-1000 (Figure 4).

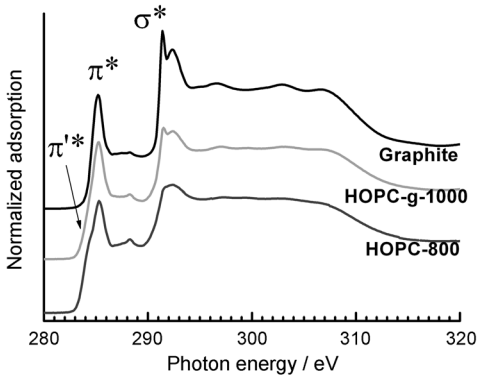

Figure 4. Carbon K-edge X-ray absorption near-edge spectra of graphite, HOPC-800, and HOPC-g-1000.

Similar to graphite, the XANES spectrum of HOPC-g-1000 shows a sharp $1s \rightarrow \pi^*$ peak at 285.2 eV and the typical line shape of the $1s \rightarrow \sigma^*$ edge at around 291.4 eV, which corresponds to fingerprints of sp^2-hybridized carbon atoms.[18,41] Interestingly, the line shape of the $1s \rightarrow \sigma^*$ edge is replaced by

a smooth edge in the spectrum of HOPC-800, which is consistent with a disordered sp^2 matrix and amorphous phase. In addition, the features in the 287–290 eV region can be assigned to C=O π^*, C–O σ^*, or C–H σ^* transitions; these are related to oxygenated surface functionalities, oxygen contaminated by atmospheric exposure, or the presence of hydrogen after incomplete pyrolysis of the hydrocarbon precursors.[18,41–44] Energy-dispersive X-ray spectroscopy (EDS) analysis shows that HOPC-g-1000 contained up to 1.3 wt% oxygen. Clearly, a shoulder at 284.3 eV, derived from the $1s \rightarrow \pi^*$ pre-edge region can be observed and ascribed to distorted sp^2 bonds (π'^*).[41] The distorted sp^2 bonds (π'^*) diminish when the temperature increases to 1000 °C; however, the shoulder in the spectrum of HOPC-g-1000 remains, highlighting the survival of the residual disordered phase. Here, the appearance of these peaks in HOPC-g-1000 is consistent with amorphous and graphitic carbon observed in the XRD pattern and TEM image. It can be concluded that the microstructures of HOPC-800 are amorphous matrices, in which prevalent sp^2-hybridized carbon atoms tend to be reorganized into well-ordered graphitic structures around the surface of metallic Ni when the temperature increases to 1000 °C during catalytic graphitization.

To understand the thermal properties and graphitic carbon content in 3D HOPC materials, thermogravimetric analysis (TGA) and simultaneous differential thermal analysis (SDTA) were employed to determine the change in weight loss and heat flow in air (Figure 5). Both HOPC-800 and HOPC-g-1000

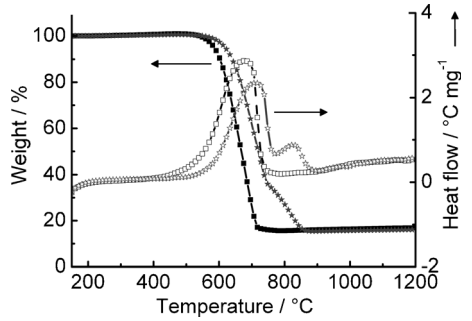

Figure 5. TGA (filled symbols) and SDTA (empty symbols) curves of HOPC-800 (■) and HOPC-g-1000 (★) recorded in air.

are stable until 500 °C. Almost complete weight loss (84.4%) of HOPC-800 is observed at 740 °C. HOPC-g-1000 is more thermally resistant, and a weight loss of 64 wt% appears at 740 °C, which is mainly contributed to amorphous carbon. Further weight loss of 21 wt% occurs in the temperature range of 740–900 °C, presumably attributed to oxidation of graphitic carbon. Finally, a residual 15 wt% is left at 1200 °C, which is mainly in the form of NiO (corresponding to 11.8 wt% of metallic Ni). The SDTA curve of HOPC-g-1000 shows two peaks centered at 710 and 830 °C (Figure 5), indicating the coexistence of amorphous and graphitic carbons, which is in good agreement with XRD and TEM characterizations.

The N_2 adsorption–desorption isotherms and pore size distributions (PSDs; Figure 6) of 3D HOPC materials with 2D hexag-

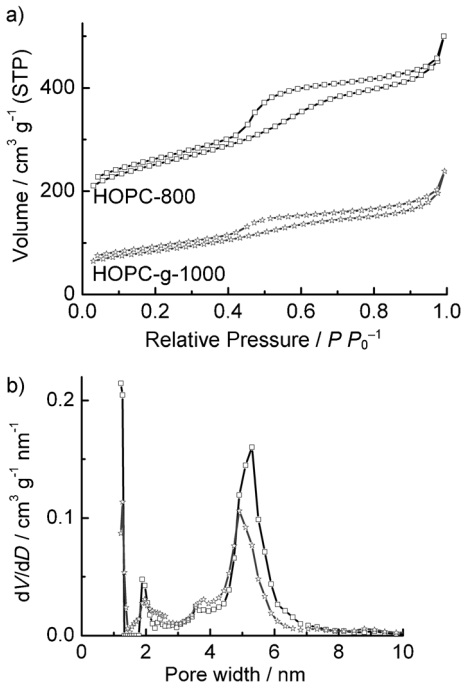

Figure 6. a) N_2 adsorption–desorption isotherms and b) PSDs of HOPC-800 (□) and HOPC-g-1000 (☆).

onally ordered mesostructures show typical type IV curves with a clear H2-type hysteresis loop in the relative pressure (P/P_0) range of 0.4–0.7, showing a narrow distribution of the mesoporous characteristics. In addition, further N_2 uptake is observed at a relatively high pressure of $P/P_0 = 0.9$–1.0, which can be attributed to the presence of macropores. The specific surface areas of HOPC-800 and HOPC-g-1000 are 528 and 296 $m^2 g^{-1}$, respectively. Using the nonlocal density functional theory (NLDFT) method confirms that the specific surface areas of the HOPC-800 and HOPC-g-1000 are 555 and 313 $m^2 g^{-1}$, respectively. The decrease in surface area is mainly attributed to destruction of porosity and the formation of nonporous graphitic carbon around the surface of metallic Ni nanoparticles during the high-temperature graphitization process. In addition, changes in micropore surface areas (from 268 to 61 $m^2 g^{-1}$), total pore volumes (from 0.47 to 0.37 $cm^3 g^{-1}$), and micropore volumes (from 0.12 to 0.03 $cm^3 g^{-1}$) of HOPC-800 and HOPC-g-1000 also confirm the destruction of porosity (Table 1). The formation of nonporous graphitic domains

Table 1. The pore texture properties of HOPC-800 and HOPC-g-1000 materials.[a]

Sample	S_{BET} [$m^2 g^{-1}$]	S_{mi} [$m^2 g^{-1}$] ([%])	V_t [$cm^3 g^{-1}$]	V_{mi} [$cm^3 g^{-1}$] ([%])
HOPC-800	528	268 (51)[b]	0.47	0.12 (26)[b]
HOPC-g-1000	296	61 (21)[b]	0.37	0.03 (8)[b]

[a] S_{BET} = total specific surface areas, S_{mi} = microporous surface area, V_t = total pore volume, V_{mi} = micropore volume. [b] Percentages of microporous specific surface areas and microporous volume in the surface area and pore volume, respectively.

around the surface of metallic Ni occurs through the dissolution of amorphous carbon into metallic Ni nanoparticles, followed by the surface diffusion of carbon atoms, and finally assembly into graphitic carbon.[29,38–40] It is reasonable to see why the pores are partially collapsed: catalytic graphitization with Ni nanoparticles as catalysts results in an even higher electrical conductivity, but causes the collapse of the pores.

To accurately describe the PSD for a material with micro- and mesopores, NLDFT and Monte-Carlo methods are utilized. HOPC-800 and HOPC-g-1000 exhibit apparent bimodal patterns with micropore sizes of 1.2 nm and mesopore sizes of about 5.0 nm. The peak intensities and mesopore sizes decrease after the graphitization process at 1000 °C, suggesting the collapse of porous structures and shrinkage of the mesopores. The PSD between 1.2 and 5.0 nm can be divided into two minor regions: 1.7–2.7 and 3.0–4.0 nm. In addition, the percentages of micro- (< 2 nm), meso- (2–50 nm), and macroporous (> 50 nm) surface areas (volumes) in HOPC-g-1000, deduced from Barrett–Joyner–Halenda (BJH) cumulative adsorption surface area and pore volume curves shown in Figure S4 in the Supporting Information, are 20 (6), 63 (63), and 31% (26%), respectively. The synthesized 3D HOPC materials exhibit superior hierarchical porosities, including 3D, well-interconnected, ordered, macroporous frameworks with 2D hexagonally ordered mesostructures with uniform meso- and micropores. These superior hierarchical porosities can provide fast electrolyte diffusion pathways, low ion-transport resistance, good electrolyte accessibility, and high-rate capacitance performance, resulting in strengthening of charge accommodation in micropores.

Electrochemical properties

Cyclic voltammetry (CV) was performed to evaluate the capacitance performance of 3D HOPC materials in a three-electrode cell by varying the scanning rates between 3 and 500 mV s^{-1} with a potential window of 1.0 V. As shown in Figure 7, the CV curves present typical capacitive behavior, as evidenced by their nearly rectangular voltammograms, indicating good charge propagation and facile ion transport within the electrodes. When the scan rate reaches 100 mV s^{-1}, the shape of the CV curves retains a rectangular shape and does not change dramatically. A totally distorted rectangular shape of the CV curve is observed when the scan rate increases to 500 mV s^{-1}. The hierarchically ordered porous structures have significantly lower resistance to ion transport during high-rate charge and discharge processes. The small reduction–oxidation peaks visible in the cyclic voltammograms at 0 and 1.0 V [vs. a reversible hydrogen electrode (RHE)] at the slowest scan rate are believed to originate from oxygen-containing functional groups remaining in the HOPC electrodes. Such peaks completely disappear at a scan rate of 50 mV s^{-1}, suggesting relatively slow rate pseudocapacitance or electrochemical redox reactions.[1,4] The gravimetric specific capacitances are normalized to the specific Brunauer–Emmett–Teller (BET) surface area to elucidate the accessibilities of carbon surface to electrolyte. Figure 7c summarizes the changes in specific capacitances of HOPC electrodes deduced from CV measurements recorded at various scan rates. The specific capacitance of HOPC-800 decreases from 21.2 μF cm^{-2} (111.9 F g^{-1}) at 3 mV s^{-1} to 12.3 μF cm^{-2} (64.9 F g^{-1}) at 200 mV s^{-1}, which corresponds to a capacitance retention of 58%. By comparison, the specific capacitance of HOPC-g-1000 decreases from 24.8 μF cm^{-2} (73.4 F g^{-1}) at 3 mV s^{-1} to 16.0 μF cm^{-2} (47.1 F g^{-1}) at 200 mV s^{-1}, and the capacitance retention is 65%. Such decreases in specific capacitances are common for porous carbons and are likely to originate from insufficient time available for ion transport and adsorption inside the smallest pores (such as micropores and small mesopores).

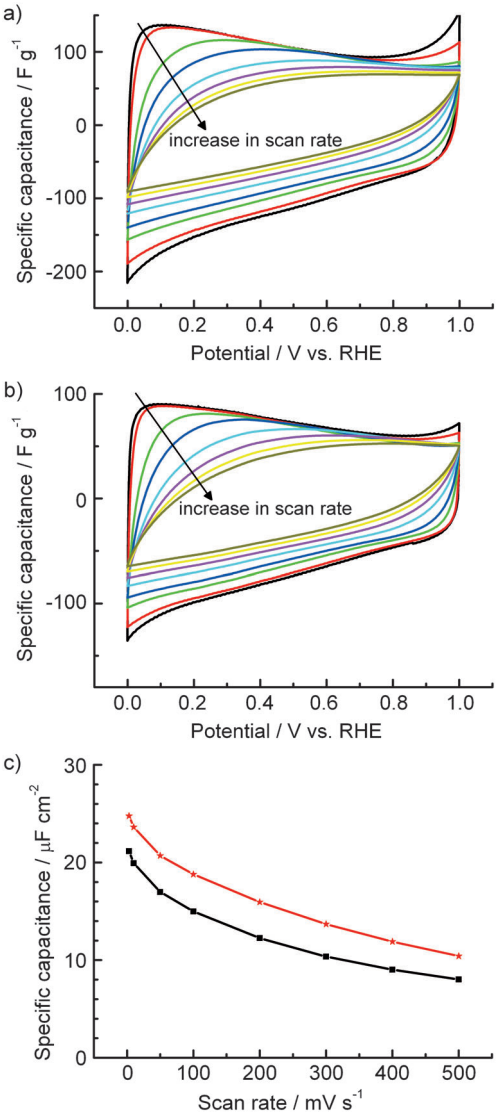

Figure 7. The CV curves of a) HOPC-800 and b) HOPC-g-1000 electrodes at various scan rates ranging from 3 to 500 mV s^{-1} (—— 3, —— 10, —— 50, —— 100, —— 200, —— 300, —— 400, and —— 500 mV s^{-1}). c) The specific capacitance of HOPC electrodes (■ HOPC-800; ★ HOPC-g-1000) as a function of scan rate.

It is noteworthy that the estimated capacitance per surface area for HOPC-800 and HOPC-g-1000 can be up to 21.1 and 24.8 μF cm^{-2} at 3 mV s^{-1}, respectively, which is close to an average value of 25 μF cm^{-2} and higher than that of conventional

porous carbons (10–12 μF cm^{-2}), graphitic porous carbons (12–13 μF cm^{-2}), hierarchically porous carbons (7–15 μF cm^{-2}), carbon nanofiber (CNF)@CNT composites (14 μF cm^{-2}), and modified graphene (19 μF cm^{-2}) in aqueous electrolytes at low scan rates.[1,8,20,24,45,46] When scan rates increase, the specific capacitances of HOPC-800 and HOPC-g-1000 decrease from 12.3 and 16.0 μF cm^{-2} at 200 mV s^{-1} to 8.0 and 10.4 μF cm^{-2} at 500 mV s^{-1}, respectively. The results indicate that the capacitance retention (58%) of HOPC-800 is lower than that (65%) of HOPC-g-1000 as the scan rate increases from 3 to 200 mV s^{-1}. However, as it increases from 200 to 500 mV s^{-1}, the capacitance retentions of HOPC-800 and HOPC-g-1000 are similar. According to a previous report,[6] the results show that the contribution from micropores (< 2 nm, C_{micro}) to the observed capacitance in aqueous electrolytes (1.0 M H_2SO_4) is lower than that of other larger pores (> 2 nm, C_{ext}) at high current densities. In addition, C_{ext} does not show a pronounced change with increasing current density, but C_{micro} shows a gradual decrease with increasing current density. It can be concluded that HOPC-g-1000 materials have better electrolyte accessibility, which is attributed to less microporosity, higher conductivity, and 3D hierarchically ordered porous structures, and these materials are more suitable for high-rate operations. However, the volumetric capacitance was too small for industrial applications because of the large proportion of pores, especially macropores.

To further quantitatively evaluate the rate performances and accurately determine the specific capacitances of 3D HOPC electrodes, galvanostatic (constant current) charge–discharge cycles were measured from 1 to 10 A g^{-1}. The specific capacitances are calculated from the discharge curves of the galvanostatic profiles (Figure 8a and b). All charge–discharge curves of the HOPC electrodes at various current densities are linear and symmetrical, indicating that the electrodes possess excellent charge–discharge reversibility. HOPC-800 exhibits a specific capacitance of 20.7 μF cm^{-2} (109.4 F g^{-1}) at 1 A g^{-1} and 16.8 μF cm^{-2} (88.8 F g^{-1}) at 10 A g^{-1} (retention of 81%), whereas HOPC-g-1000 exhibits specific capacitances of 22.5 μF cm^{-2} (66.7 F g^{-1}) and 18.3 μF cm^{-2} (54.2 F g^{-1}) at 1 and 10 A g^{-1}, respectively, with a capacitance retention of 81%, displaying superior ion-transport properties and excellent performance of 3D HOPC electrodes (Figure 8c).

Facilitated ion-transport kinetics within hierarchically ordered porous structures was further studied by performing electrochemical impedance spectroscopy (EIS). Nyquist plots of the HOPC electrodes (Figure 9a) show a semicircle in the high-frequency region followed by a sloping straight line. The semicircle in the high-frequency region represents an electrochemistry-controlled process, whereas the straight line in the low-frequency region is the electrolyte diffusion-controlled reaction. The intercept at the real impedance (Z') axis in the high-frequency region is related to internal resistance (R_s), which includes the resistance of the bulk electrolyte, the intrinsic resistance of HOPC materials, and contact resistance at the interface of HOPC materials/Ni foam current collector. The R_s values of HOPC-800 and HOPC-g-1000 are 0.22 (8.8) and 0.10 Ω (5.9 kHz), respectively; this demonstrates that the resistance of

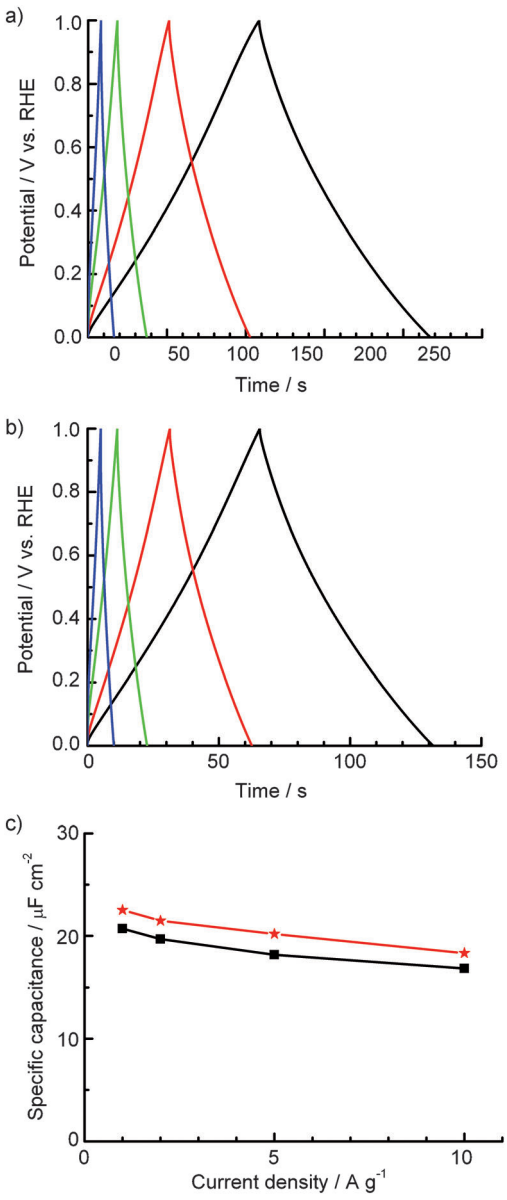

Figure 8. The galvanostatic charge–discharge curves of a) HOPC-800 and b) HOPC-g-1000 electrodes at various current densities ranging from 1 to 10 A g^{-1} (—— 1, —— 2, —— 5, —— 10 A g^{-1}). c) The specific capacitance of HOPC electrodes as a function of current density (■ HOPC-800; ★ HOPC-g-1000).

bulk electrolyte transport between the reference and working electrodes is very low. The diameter of the semicircle on the Z' axis usually indicates the charge-transfer resistance (R_{ct}) at the interface between the electrode and electrolyte and is related to the porous structure and conductivity of the electrode materials. The R_{ct} values of HOPC-800 and HOPC-g-1000 are 0.45 and 0.36 Ω and are much lower than that (2.5 Ω) of carbon materials with hierarchical architectures and wormhole-like mesostructures.[24] At low-frequency ranges (less than 1 Hz), the inclined lines for HOPC materials are closer to the theoretical vertical line and show characteristic features of pure capacitive behavior, indicating better pore accessibility for the electrolyte in the HOPC materials.[24] According to the above EIS re-

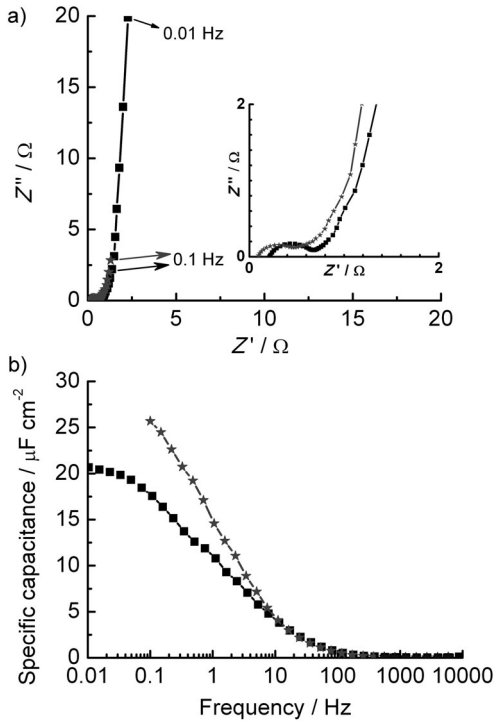

Figure 9. a) Nyquist plots and b) the specific capacitance–frequency dependence of HOPC-800 (■) and HOPC-g-1000 (★) electrodes.

sults, HOPC materials with 3D, hierarchically ordered, porous structures, especially HOPC-g-1000, have improved electrical conductivity, which can promote the electron and ion transport.

The frequency response of capacitance (Figure 9b) of HOPC electrodes reveals the significant influence of the hierarchically porous structures on the rate of ion transport. Clearly, the capacitance decreases gradually with increasing frequency, which indicates the limitation of ion transport at high frequencies. This is a common feature for porous carbon electrodes. The capacitance of the HOPC-g-1000 electrode nearly approaches saturation below 0.1 Hz, which implies that ion adsorption can reach equilibrium within 10 s, which is similar or slightly faster than that in commercial devices (generally in the range of 10–100 s). Comparing the frequencies at which the capacitance is 50% of its maximum value ($f_{0.5}$), we clearly see that the HOPC electrodes exhibit the fastest frequency response with $f_{0.5} \approx 1$ Hz, corresponding to the characteristic relaxation time constant of 1 s. The operating frequency of HOPC electrodes (1 Hz) is similar to or higher than that of microporous carbons (0.03–0.1 Hz), ordered mesoporous carbons, and hierarchically porous carbons.[47,48]

To understand the electrochemical cycling stability of HOPC electrodes, the cycling stabilities were evaluated in 6 M KOH at a scan rate of 200 mV s^{-1}, as shown in Figure 10. The specific capacitances of HOPC-800 and HOPC-g-1000 do not fade over thousands of consecutive cycles; this clearly indicates excellent electrochemical stability and potential applications of the HOPC materials in energy-storage devices.

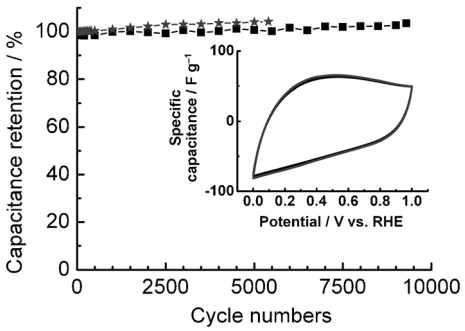

Figure 10. The cycling stability of HOPC electrodes (■ HOPC-800, ★ HOPC-g-1000) at a scan rate of 200 mV s^{-1}. The insert shows the 1st (——) and 5400th (——) CV curves of HOPC-g-1000.

Conclusions

We successfully demonstrated the synthesis of 3D, hierarchically ordered, porous carbons without/with partially graphitic nanostructures by a simple one-pot dual-templating reaction with evaporation-induced self-assembly for applications in electrochemical supercapacitors. The synthesized 3D HOPC-g-1000 materials have good graphitization domains and superior hierarchical porosities, including 3D, interconnected, ordered fcc macropores (300 nm) and macroporous windows (170 nm); hexagonally ordered mesopores (5.0 nm); and useful micropores (1.2 nm). HOPC-g-1000, with partially graphitic nanostructures, leads to a low specific surface area (296 m^2 g^{-1}) and a low gravimetric specific capacitance (73.4 F g^{-1} at 3 mV s^{-1}), but improved electrical conductivity, better rate performance, higher electrolyte accessibility (24.8 μF cm^{-2} at 3 mV s^{-1}), faster frequency response ($\approx$1 Hz), and excellent cycling performance (>5400 cycles). The specific capacitance per surface area is higher than that of conventional porous carbons, graphitic porous carbons, hierarchically porous carbons, CNTs, and modified graphene (10–19 μF cm^{-2}). Fortunately, the macropore size can be tuned for the optimization of HOPC materials in applications requiring a desired balance of energy and power densities. The results obtained clearly demonstrate the feasibility of using 3D HOPC materials without/with partially graphitic nanostructures. These materials would also be useful models to elucidate transport limitation and the roles of ordered pores and graphitic carbons in sustainable catalysis, catalyst supports, and energy-storage materials. In the future, the quantitative modeling of the mass transport properties in 3D HOPCs in the above applications by tuning the macropore size can be intensively studied.

Experimental Section

Preparation of 3D, hierarchically ordered, porous carbons with partially graphitic nanostructures

Solutions of 50 wt% PF resins in ethanol were prepared by performing a basic polymerization method. Monodisperse polystyrene (PS) latex spheres were prepared by emulsifier-free emulsion polymerization. Detailed experimental details for the synthesis of PF resins and PS latex spheres are provided in the Supporting Infor-

mation. The 3D HOPC materials were fabricated by performing a one-pot dual-templating method with evaporation-induced self-assembly. Typically, triblock copolymer F127 (6.0 g), 50 wt% PF precursors (12.0 g), 20 wt% $NiCl_2$ solution (12.0 g), and 50 wt% solution of PS latex (10.0 g) in ethanol were added and then stirred vigorously for 1.0 h at room temperature. The homogenous mixture was transferred into Petri dishes at room temperature for 24.0 h and then at 60 °C for 24.0 h. After drying, the monoliths were heated at 100 °C for 24.0 h. The as-prepared monoliths were scraped from the Petri dishes. Subsequently, the monoliths were calcined to 600 °C at a heating rate of 1.0 °C min^{-1} under a flow of 5% H_2/N_2 at 100 mL min^{-1} in a tubular furnace. Finally, the temperature was ramped to the desired value (800 or 1000 °C) at a heating rate of 5.0 °C min^{-1} and maintained for 3.0 h.

Characterization and measurements

Detailed characterization for the materials is provided in the Supporting Information. The XRD patterns of HOPC materials were examined by using an X-ray diffractometer (XRD, Bruker NEW D8 ADVANCE, Germany) with a Lynx eye high-speed strip detector and Ni-filtered CuK_α radiation ($\lambda = 1.5406$ Å). TEM images and energy-dispersive X-ray spectroscopy measurements were obtained by using a Philips CM200 LaB_6 microscope. The surface morphology of HOPC was examined by using JEOL JSM-6330F and Hitachi S4800 scanning electron microscopes. Soft XANES spectra of the carbon K-edge were measured in total X-ray fluorescence yield mode at room temperature by using a BL-20A instrument at the National Synchrotron Radiation Research Center (NSRRC, Hsinchu, Taiwan). N_2 adsorption–desorption isotherms were collected at 77 K by using an N_2 adsorption analyzer (Quantachrome, Autosorb-6B). The Brunauer–Emmett–Teller (BET) method was utilized to calculate the total specific surface areas (S_{BET}). To accurately describe the pore size distribution (PSD) for a material with micro- and mesopores, nonlocal density functional theory and Monte-Carlo methods were utilized. The total pore volumes (V_t) were estimated from the adsorbed amount at a relative pressure (P/P_0) of 0.994. The micropore volumes (V_{mi}) and micropore surface areas (S_{mi}) were calculated by using the *t*-plot method. The thermal properties of the products were determined by using a Mettler Toledo TGA/SDTA851 analyzer (Switzerland).

Electrochemical measurements

A detailed preparation method of the working electrodes is provided in the Supporting Information. Prior to electrochemical measurements, the working electrodes were impregnated with 6.0 M KOH electrolyte solution for 24 h. CV and EIS data were obtained by using a VSP BioLogic electrochemical workstation. The three-electrode system in a beaker-type cell at room temperature consisted of a working electrode, a platinum plate counter electrode with an exposed area equal to 2 cm^2, and a reversible hydrogen electrode (HydroFlex, Gaskatel). A 6.0 M KOH aqueous solution was used as the electrolyte. To minimize errors resulting from ohmic potential drop in the electrolytes, the tip of RHE was set at a distance of 1–2 mm from the surface of the working electrode. The gravimetric specific capacitance (C_s) was calculated from the cyclic voltammograms and galvanostatic discharge process results were calculated according to Equations (1) and (2):

$$C_s = (\int dVI)/(2\,v\Delta V) \quad (1)$$

$$C_s = I\Delta t/\Delta V \quad (2)$$

in which v is the scan rate (V s^{-1}), ΔV is the potential window (*V*), I is the current density (A g^{-1}), and Δt is the discharge time. The EIS measurements were performed in the frequency range from 100 kHz to 100 mHz at an open-circuit voltage with a 10 mV AC amplitude. The gravimetric capacitance was also calculated according to Equation (3):

$$C_s = -1/[2\,\pi f\, Im(Z)m] \quad (3)$$

in which f is the operating frequency (in Hz), $Im(Z)$ is the imaginary part of the electrode resistance (in Ω), and m is the mass of the active material.

Acknowledgements

The work was supported by the National Science Council, Taiwan (NSC99-2113M-007-007-MY3) and the EnerChem project of the Max Planck Society. We gratefully acknowledge gas sorption and XRD measurements from Gisela Lorenz and Edith Kitzelmann, and facilities from the National Synchrotron Radiation Research Center (NSRRC). C.H.H. greatly appreciates support by a Sandwich Program Spring Session 2011 scholarship from the Deutschen Akademischen Austausch Dienst (DAAD, Germany) and the National Science Council (NSC, Taiwan).

Keywords: carbon · electrochemistry · energy storage · nanostructures · supercapacitors

[1] E. Frackowiak, F. Beguin, *Carbon* **2001**, *39*, 937 – 950.
[2] P. Simon, Y. Gogotsi, *Nat. Mater.* **2008**, *7*, 845 – 854.
[3] C. Liu, F. Li, L. P. Ma, H. M. Cheng, *Adv. Mater.* **2010**, *22*, E28 – E62.
[4] D. S. Su, R. Schlögl, *ChemSusChem* **2010**, *3*, 136 – 168.
[5] J. Liu, G. Z. Cao, Z. G. Yang, D. H. Wang, D. Dubois, X. D. Zhou, G. L. Graff, L. R. Pederson, J. G. Zhang, *ChemSusChem* **2008**, *1*, 676 – 697.
[6] M. Inagaki, H. Konno, O. Tanaike, *J. Power Sources* **2010**, *195*, 7880 – 7903.
[7] L. L. Zhang, X. S. Zhao, *Chem. Soc. Rev.* **2009**, *38*, 2520 – 2531.
[8] D. W. Wang, F. Li, M. Liu, G. Q. Lu, H. M. Cheng, *Angew. Chem.* **2008**, *120*, 379 – 382; *Angew. Chem. Int. Ed.* **2008**, *47*, 373 – 376.
[9] F. B. Su, X. S. Zhao, Y. Wang, J. H. Zeng, Z. C. Zhou, J. Y. Lee, *J. Phys. Chem. B* **2005**, *109*, 20200 – 20206.
[10] E. Raymundo-Piñero, M. Cadek, M. Wachtler, F. Béguin, *ChemSusChem* **2011**, *4*, 943 – 949.
[11] Z. J. Fan, J. Yan, L. J. Zhi, Q. Zhang, T. Wei, J. Feng, M. L. Zhang, W. Z. Qian, F. Wei, *Adv. Mater.* **2010**, *22*, 3723 – 3728.
[12] X. C. Zhao, A. Q. Wang, J. W. Yan, G. Q. Sun, L. X. Sun, T. Zhang, *Chem. Mater.* **2010**, *22*, 5463 – 5473.
[13] L. Zhao, L. Z. Fan, M. Q. Zhou, H. Guan, S. Y. Qiao, M. Antonietti, M. M. Titirici, *Adv. Mater.* **2010**, *22*, 5202 – 5206.
[14] W. Li, F. Zhang, Y. Q. Dou, Z. X. Wu, H. J. Liu, X. F. Qian, D. Gu, Y. Y. Xia, B. Tu, D. Y. Zhao, *Adv. Energy Mater.* **2011**, *1*, 382 – 386.
[15] J. Yan, T. Wei, B. Shao, Z. J. Fan, W. Z. Qian, M. L. Zhang, F. Wei, *Carbon* **2010**, *48*, 487 – 493.
[16] J. X. Wang, C. F. Xue, Y. Y. Lv, F. Zhang, B. Tu, D. Y. Zhao, *Carbon* **2011**, *49*, 4580 – 4588.
[17] C. H. Huang, R. A. Doong, *Microporous Mesoporous Mater.* **2011**, *142*, 473 – 480.
[18] C. H. Huang, D. Gu, D. Y. Zhao, R. A. Doong, *Chem. Mater.* **2010**, *22*, 1760 – 1767.
[19] G. H. Xu, C. Zheng, Q. Zhang, J. Q. Huang, M. Q. Zhao, J. Q. Nie, X. H. Wang, F. Wei, *Nano Res.* **2011**, *4*, 870 – 881.

[20] E. Frackowiak, *Phys. Chem. Chem. Phys.* **2007**, *9*, 1774 – 1785.
[21] Z. Chen, J. Wen, C. Yan, L. Rice, H. Sohn, M. Shen, M. Cai, B. Dunn, Y. Lu, *Adv. Energy Mater.* **2011**, *1*, 551 – 556.
[22] C. D. Liang, Z. J. Li, S. Dai, *Angew. Chem.* **2008**, *120*, 3754 – 3776; *Angew. Chem. Int. Ed.* **2008**, *47*, 3696 – 3717.
[23] J. Lee, J. Kim, T. Hyeon, *Adv. Mater.* **2006**, *18*, 2073 – 2094.
[24] Y. R. Liang, F. X. Liang, D. C. Wu, Z. H. Li, F. Xu, R. W. Fu, *Phys. Chem. Chem. Phys.* **2011**, *13*, 8852 – 8856.
[25] Y. R. Liang, D. C. Wu, R. W. Fu, *Langmuir* **2009**, *25*, 7783 – 7785.
[26] F. J. Li, M. Morris, K. Y. Chan, *J. Mater. Chem.* **2011**, *21*, 8880 – 8886.
[27] Z. L. Wang, X. B. Zhang, X. J. Liu, M. F. Lv, K. Y. Yang, J. Meng, *Carbon* **2011**, *49*, 161 – 169.
[28] W. J. Gao, Y. Wan, Y. Q. Dou, D. Y. Zhao, *Adv. Energy Mater.* **2011**, *1*, 115 – 123.
[29] C. H. Huang, R. A. Doong, D. Gu, D. Y. Zhao, *Carbon* **2011**, *49*, 3055 – 3064.
[30] S. W. Woo, K. Dokko, H. Nakano, K. Kanamura, *J. Mater. Chem.* **2008**, *18*, 1674 – 1680.
[31] Z. Y. Wang, E. R. Kiesel, A. Stein, *J. Mater. Chem.* **2008**, *18*, 2194 – 2200.
[32] Y. H. Deng, C. Liu, T. Yu, F. Liu, F. Q. Zhang, Y. Wan, L. J. Zhang, C. C. Wang, B. Tu, P. A. Webley, H. T. Wang, D. Y. Zhao, *Chem. Mater.* **2007**, *19*, 3271 – 3277.
[33] A. H. Lu, W. C. Li, E. L. Salabas, B. Spliethoff, F. Schuth, *Chem. Mater.* **2006**, *18*, 2086 – 2094.
[34] R. W. Fu, T. F. Baumann, S. Cronin, G. Dresselhaus, M. S. Dresselhaus, J. H. Satcher, *Langmuir* **2005**, *21*, 2647 – 2651.
[35] F. Xu, R. J. Cai, Q. C. Zeng, C. Zou, D. C. Wu, F. Li, X. E. Lu, Y. R. Liang, R. W. Fu, *J. Mater. Chem.* **2011**, *21*, 1970 – 1976.
[36] N. Amini, K. F. Aguey-Zinsou, Z. X. Guo, *Carbon* **2011**, *49*, 3857 – 3864.
[37] J. Q. Huang, Q. Zhang, M. Q. Zhao, F. Wei, *Carbon* **2010**, *48*, 1441 – 1450.
[38] J. P. Tessonnier, D. S. Su, *ChemSusChem* **2011**, *4*, 824 – 847.
[39] A. Rinaldi, J. P. Tessonnier, M. E. Schuster, R. Blume, F. Girgsdies, Q. Zhang, T. Jacob, S. B. A. Hamid, D. S. Su, R. Schlögl, *Angew. Chem.* **2011**, *123*, 3371 – 3375; *Angew. Chem. Int. Ed.* **2011**, *50*, 3313 – 3317.
[40] Q. Zhang, J. Q. Huang, M. Q. Zhao, W. Z. Qian, F. Wei, *ChemSusChem* **2011**, *4*, 864 – 889.
[41] R. Larciprete, S. Lizzit, S. Botti, C. Cepek, A. Goldoni, *Phys. Rev. B* **2002**, *66*, 121 402.
[42] M. Abbas, Z. Y. Wu, J. Zhong, K. Ibrahim, A. Fiori, S. Orlanducci, V. Sessa, M. L. Terranova, I. Davoli, *Appl. Phys. Lett.* **2005**, *87*, 051923.
[43] S. Banerjee, T. Hemraj-Benny, M. Balasubramanian, D. A. Fischer, J. A. Misewich, S. S. Wong, *ChemPhysChem* **2004**, *5*, 1416 – 1422.
[44] A. Kuznetsova, I. Popova, J. T. Yates, M. J. Bronikowski, C. B. Huffman, J. Liu, R. E. Smalley, H. H. Hwu, J. G. G. Chen, *J. Am. Chem. Soc.* **2001**, *123*, 10699 – 10704.
[45] M. D. Stoller, S. J. Park, Y. W. Zhu, J. H. An, R. S. Ruoff, *Nano Lett.* **2008**, *8*, 3498 – 3502.
[46] J. Zhang, Y. S. Hu, J. P. Tessonnier, G. Weinberg, J. Maier, R. Schlögl, D. S. Su, *Adv. Mater.* **2008**, *20*, 1450 – 1455.
[47] W. Xing, C. C. Huang, S. P. Zhuo, X. Yuan, G. Q. Wang, D. Hulicova-Jurcakova, Z. F. Yan, G. Q. Lu, *Carbon* **2009**, *47*, 1715 – 1722.
[48] L. Wei, M. Sevilla, A. B. Fuertes, R. Mokaya, G. Yushin, *Adv. Energy Mater.* **2011**, *1*, 356 – 361.

Received: October 5, 2011
Revised: December 7, 2011
Published online on ■■ ■■, 0000

C.-H. Huang, Q. Zhang, T.-C. Chou, C.-M. Chen, D. S. Su, R.-A. Doong**

■■ – ■■

Three-Dimensional Hierarchically Ordered Porous Carbons with Partially Graphitic Nanostructures for Electrochemical Capacitive Energy Storage

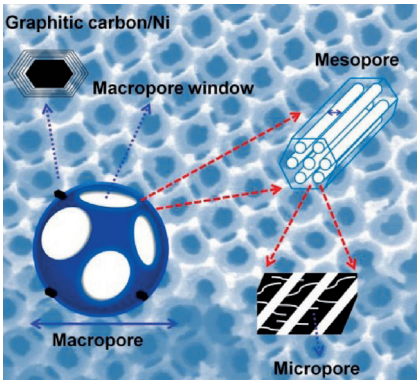

Open up! A three-dimensional hierarchically-ordered porous carbon with partially graphitic nanostructure has been designed, fabricated, and explored as a supercapacitor electrode (see picture). The macropores, interconnected porous structures, and meso/micropores are used as ion-buffering reservoirs, ion-transport channels, and charge-storage materials, respectively, and are expected to be advanced energy materials for high-rate supercapacitors.

